Using the discrete element method to simulate brittle fracture in the indentation of a silica glass with a blunt indenter

Damien André[a], Mohamed Jebahi[b], Ivan Iordanoff[a], Jean-luc Charles[a], Jérôme Néauport[c]

[a] *Arts & Métiers ParisTech, I2M-DuMAS-MPI, UMR 5295 CNRS F-33405, Talence, France*
[b] *Univ. Bordeaux 1, I2M-DuMAS, UMR 5295 CNRS F-33405, Talence, France*
[c] *Commissariat à l'Énergie Atomique, Centre d'Études Scientifiques et Techniques d'Aquitaine, BP 2, 33114 Le Barp, France*

Abstract

The mechanical behavior of materials is usually simulated by a continuous mechanics approach. However, non-continuous phenomena such as multi-fracturing cannot be accurately simulated using a continuous description. The discrete element method (DEM) naturally accounts for discontinuities and is therefore a good alternative to the continuum approach.

This study continues previous work in which a DEM model was developed to quantitatively simulate an elastic material with the cohesive beam bond model. The simulation of brittle cracks is now tackled. This goal is attained by computing a failure criterion based on an equivalent hydrostatic stress. This microscopic criterion is then calibrated to fit experimental values of the macroscopic failure stress. The simulation results are compared to experimental results of indentation tests in which a spherical indenter is used to load a silica glass, which is considered to be a perfectly brittle elastic material.

Keywords: discrete element method, DEM, calibration, silica, brittle, crack, indentation, hertzian cone.

1. Introduction

The discrete element method (DEM) can quite naturally describe a granular medium. However, computational resources are required to manage a large number of discrete elements. The method was first developed in the early 1980s (1). More recently, researchers have used this method to study damage in heterogeneous solids, such as concrete (2) or rock (3), and homogeneous materials, such as ceramics (4).

In this paper, studies are conducted on the silica glass material, which can be considered to be a homogeneous, isotropic and perfectly brittle elastic material. This research is related to the subsurface damage of silica glass due to surface polishing. In a preliminary study (5), discrete element models were used to obtain qualitatively good agreement with experiments. The current challenge is to develop a 3D DEM spherical model to quantitatively simulate silica glass as a continuous media. The first step of simulating the elastic behavior of silica (as represented by the Young's modulus and Poisson's ratio), was achieved using the cohesive beam bond model. This method was detailed in a previous paper (6).

In this study, an improvement of this method is first presented. The modification to the original method consists of increasing the number of bonds for each discrete element to improve the convergence of the numerical results. The main advantage of this modification that a better description of a continuous media is obtained at a reasonable computational cost, which only involves increasing the bond number and not the number of discrete elements.

In this work, brittle fracture is simulated using the discrete element method. Continuous mechanics laws cannot be used directly in a DEM formulation; therefore, the main challenge in using DEM is to develop a model that quantitatively fits the experimental observations of brittle phenomena, which are generally treated and analyzed within a continuous mechanics framework (7).

A preliminary task is to choose a microscopic failure criterion for the discrete element model. The main failure criteria are based on computing the bond strain (8) or stress (9). In these cases, a bond is deleted if the stress or the strain of the bond exceeds a threshold. This process mimics crack formation in a material. These thresholds are determined by calibration tests. In this

study, a novel criterion is developed based on the equivalent hydrostatic stress exerted on the discrete elements. The associated calibration procedure is also detailed.

Polishing processes can be viewed as repeated indentation by abrasives on a glass surface (10); therefore, the developed method is validated using indentation tests with spherical indenters. Spherical indenters produce a conical crack geometry. This result was first observed by Hertz (11, 12). This phenomena has been intensively studied; however, computational models are still in discussion (13, 14, 15, 16, 17). The objective of this paper is to investigate DEM as an effective alternative for studying complex cracking phenomena such as the hertzian cone crack. The numerical results from the discrete element method are compared to the experimental observations.

In this paper, the developed method is presented in four steps, as given below :

1. First, background on DEM is briefly reviewed. The integration time scheme and the elastic model are introduced. The main results given in (6) are also summarized in this section.
2. Second, a detailed procedure is presented for improving the description of a continuous media, by increasing the cardinal number of the discrete domain. These results are compared to those given in (6).
3. Third, a failure criterion and an associated calibration procedure are developed. A series of standard failure tests (tensile, bending and torsion) are simulated to validate the method.
4. Finally, indentation tests using a spherical indenter are presented. The numerical results are compared to the experimental observations and the prediction of an analytical formulation for the following characteristics :
    - the contact area between the indenter and the silica glass substrate,
    - the critical load where the fracture occurs, and
    - the cone crack geometry.

2. DEM background

In this section, the explicit time scheme and the method used to simulate the elastic behavior are described. The reader is referred to (6) for further details.

2.1. Explicit time scheme

The numerical solution is based on an explicit integration scheme that is well suited to massive DEM simulations (18) and high velocity phenomena, such as fracturing or impact. The velocity Verlet scheme is chosen for its simplicity. The discrete element orientations are described by quaternions, which are an efficient mean of computing the discrete element rotations (19, §2.5). The quaternions are normalized at every time step to prevent numerical drift.

2.2. Elastic behavior of the discrete domain

The discrete elements are connected by cohesive beams. These beams are fixed to the centers of the connected discrete elements. The beam reactions are computed using the material strength theory for Euler-Bernoulli beams (20) according to the relative displacements and rotations of the connected discrete elements. The cohesive beams operate in tensile, bending and torsion modes.

The beam parameter values (which are called microscopic parameters) are evaluated by fitting the tensile stress to the elastic properties values of the material to simulated (which are called macroscopic properties)[1]. The beam parameter values are stable when the discrete domain satisfies geometrical criteria : the geometrical isotropy, the cardinal number, the volume fraction and the fineness. That is, the same set of microscopic beam parameter values can be associated with a given material and are independent of the discrete domain morphology, in terms of the discrete element number and the sample shape. This property is the main contribution of this method. This property is illustrated in the figure 1, which shows the evolution of the macroscopic Young's modulus E_M and Poisson's ratio ν_M with the number of discrete elements in the sample. The figure 2 shows the simulated discrete samples. It appears that, for a number of discrete elements higher than 10 000, the macroscopic parameters E_M and ν_M become stable with total fluctuation amplitudes of, respectively, 3% and 2.5%.

3. A simple method for improving the elastic behavior

In the previous study, the initial discrete domain was compacted to obtain a cardinal number value of approximately six. This value was chosen to correspond to the definition of the *random close packing* (RCP) of spheres

[1] To distinguish micro from macro properties, micro parameters are denoted by 'μ' and macro parameters by 'M'.

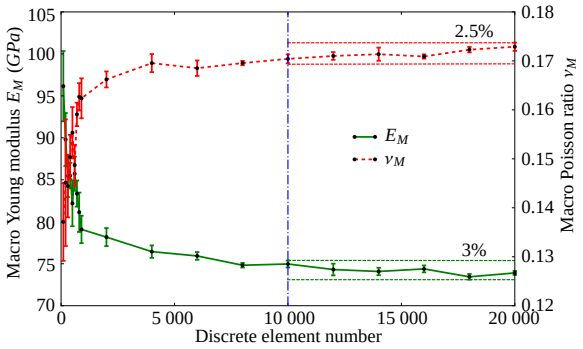

Figure 1: Macroscopic Young's modulus E_M and Poisson's ratio ν_M with the number of discrete element in the samples with a given set of microscopic parameter values.

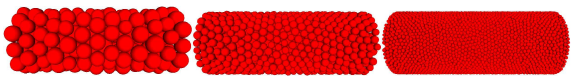

(a) 200 ED (b) 2 000 ED (c) 20 000 ED

Figure 2: Increasingly refined discrete cylindrical samples, i.e., the number of discrete elements increased from left to right.

(21). In the simulations, each contact was replaced by a cohesive beam bond. The number of cohesive bonds per discrete element was thus similar to the cardinal number of the RCP.

To improve the discrete description of a continuous media, the number of cohesive beams per discrete element was increased using the method described below :

1. An initial discrete domain was built following the RCP definition. This step was similar to the previous method.
2. A Delaunay triangulation (22, §9.3) was applied. The initial point cloud used to build the Delaunay triangulation corresponded to the discrete element centers.
3. Cohesive beam bonds were constructed for each edge obtained by the Delaunay triangulation linking two discrete element centers.

This process increased the number of cohesive beams per discrete element to thirteen.

A preliminary question concerns the level of geometric isotropy of the given discrete domain. This level should not be degraded by the Delaunay triangulation. Figure 3 shows 3D histograms of the beam direction

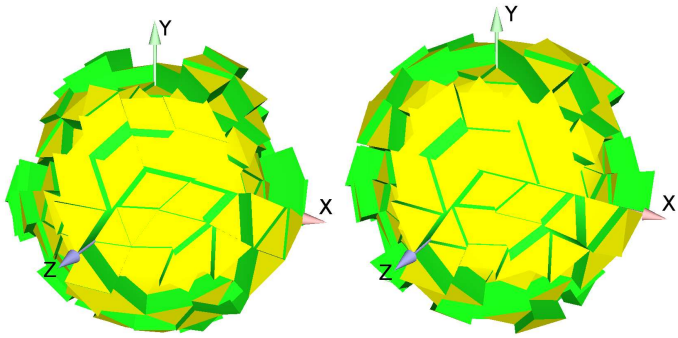

(a) Before triangulation (b) After triangulation

Figure 3: 3D histogram of cohesive beam direction before and after increasing the cardinal number.

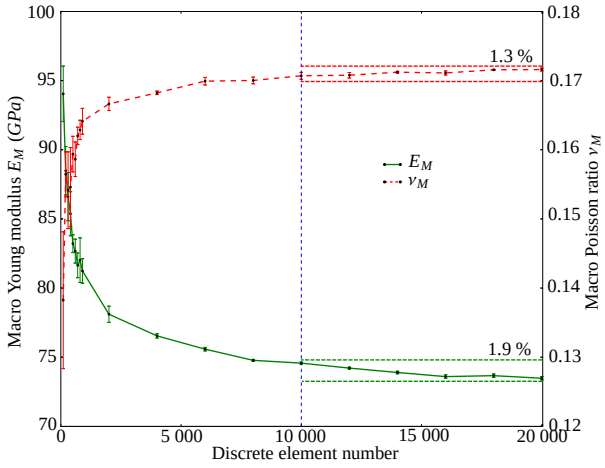

Figure 4: Macroscopic Young's modulus E_M and Poisson's ratio ν_M with the number of discrete elements the samples with an increased cardinal number.

that were obtained before and after a Delaunay triangulation. The results are quite similar. Therefore, the isotropy level was not affected by the Delaunay triangulation process.

Figure 4 shows the convergence of the elastic properties. The elastic properties are more stable than to those without the Delaunay processing (see figure 1). The macroscopic parameters E_M and ν_M were stable for more than 10 000 discrete elements with a total fluctuation amplitudes of, respectively, 1.9% and 1.3%. Also, the improved method reduced the error bars. That is, the dispersion between the elastic properties of distinct discrete samples with a same number of discrete elements were reduced.

4. The fracture criterion

Within the discrete element approach, cracks are simulated by breaking bonds that reach a particular criterion (23, 24, 25, 26, 27, 28). This approach mimics crack extension in a material. The broken bond causes an overload on the bonds localized around the broken bond. In turn, these overloaded bonds quickly reach the fracture criterion and also break.

4.1. The standard failure criterion

The main existing approaches are based on the computation of bond strains (8) or stresses (9). Strain or stress can be viewed as dual variables; therefore, these two approaches can be considered as similar to each other. The implemented failure model is based on computing the Rankine criterion, which has been suitably for brittle materials (29, §3.3) :

$$\sigma_\mu = \frac{1}{2}\left(\sigma_{\mu_{max}} + \sqrt{\sigma^2_{\mu_{max}} + 4\tau^2_{\mu_{max}}}\right) \qquad (1)$$

where :

- σ_μ is the maximal equivalent Rankine stress,
- $\sigma_{\mu_{max}}$ is the maximal normal stress and,
- $\tau_{\mu_{max}}$ is the maximal shear stress.

If the maximal equivalent Rankine stress σ_μ is higher than a calibrated value σ_{μ_f}, the cohesive beam is destroyed.

This model was investigated using a qualitative indentation test (in two dimensions) with a spherical indenter. Figure 5 illustrates a cone crack, which was produced by loading a brittle material with a spherical indenter in experiments (12, 11). Figure 6 shows the results of a qualitative 2D simulation in which the standard failure criterion defined in equation 1 was used. The simulation did not produce expected crack geometry. The fracture occurred near the indenter and propagated throughout the thickness of the material. This crack morphology did not conform to the experimental observations. In conclusion, the standard failure criterion could not reproduce the hertzian cone crack.

4.2. Development of a novel fracture criterion

A criterion is developed using the hypothesis that fused silica fracture occurs when the material is stressed in a tensile hydrostatic mode. An equivalent Cauchy stress tensor is computed for each discrete element.

Figure 5: The hertzian cone; image taken from (30).

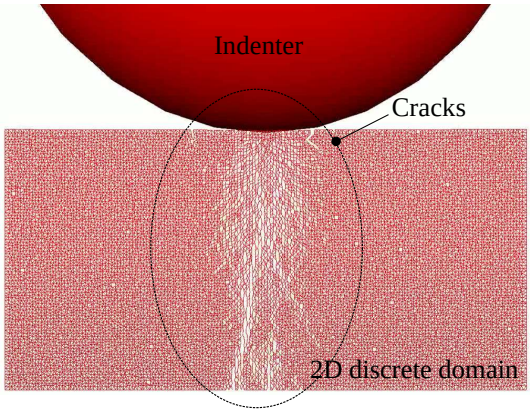

Figure 6: Qualitative 2D indentation test showing cracks produced by using the standard failure criterion.

Zhou (31) developed a method to compute a stress tensor for molecular dynamic simulations, which can formulated for the DEM as follows :

$$\bar{\sigma_i} = \frac{1}{2\Omega_i}\left(\frac{1}{2}\sum_j \vec{r}_{ij} \otimes \vec{f}_{ij} + \vec{f}_{ij} \otimes \vec{r}_{ij}\right) \qquad (2)$$

where :

- $\otimes$ is the tensor product between two vectors,
- $\bar{\sigma_i}$ is the equivalent Cauchy stress tensor of the discrete element i,
- Ω_i is the volume of the discrete element i,
- $\vec{f}_{ij}$ is the force exerted on the discrete element i by a cohesive beam that bonds the discrete element i to another discrete element j and,
- $\vec{r}_{ij}$ is the relative position vector between the center of the two bonded discrete elements i and j.

Zhou's original formulation of the Cauchy stress tensor is given below :

$$\bar{\sigma_i} = \frac{1}{2\Omega}\sum_{i\in\Omega}\sum_{j\neq i} \vec{r}_{ij} \otimes \vec{f}_{ij} \qquad (3)$$

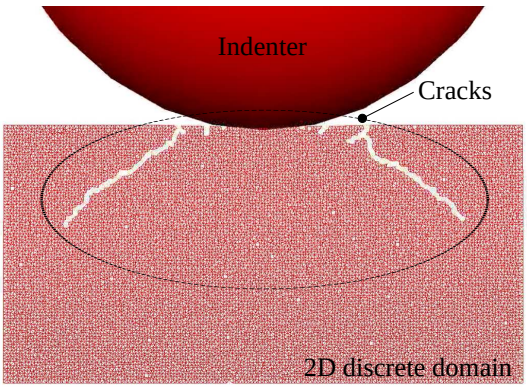

Figure 7: Qualitative 2D indentation test that shows cracks performed with the developed failure criterion.

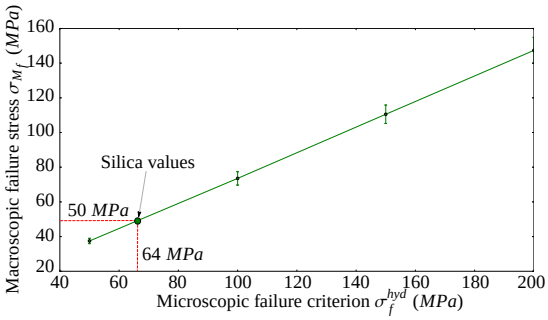

Figure 8: Evolution of the macroscopic failure stress σ_{M_f} for different values of the microscopic failure criterion σ_f^{hyd} for discrete samples containing 10 000 discrete elements.

In this formulation, the stress tensor $\bar{\sigma_i}$ is computed over a volume Ω and the forces $\vec{f_{ij}}$ are derived from Lennard-Jones potential. In this case, the computed stress tensor is symmetrical. This condition is not satisfied for discrete elements with cohesive beam bonds, because the beams are not equally distributed around a discrete element. The formulation, in equation 2, ensures that the computed stress tensor is symmetric. This computed stress tensor is used to determine the equivalent hydrostatic stress acting on discrete element *i*.

Brittle solid fracture is thought to be initiated under a tensile stress in mode I (32). Accordingly, the developed criterion assumes that fracture occurs if the hydrostatic stress is higher than a threshold value σ_f^{hyd} :

$$\frac{1}{3} trace(\bar{\sigma_i}) \geq \sigma_f^{hyd} \tag{4}$$

If the criterion is reached, all the cohesive beams bonded to the discrete element *i* are broken. In the next sections, this discrete element is called a *critical* element.

A qualitatively similar indentation test to that in the previous section was performed using the improved failure criterion. Figure 7 shows the simulation result. The crack pattern exhibits a cone geometry. In conclusion, the improved failure criterion in equation 2 provides a better description of brittle fracture and will be used in the remainder of the paper.

5. Calibration procedure

The failure criterion σ_f^{hyd} was calibrated using the same procedure described for the microscopic elastic parameters in (6). A series of failure tensile tests was processed with different values of σ_f^{hyd}. Each discrete sample consisted of approximately 10 000 discrete elements. Four distinct discrete samples were used. Figure 8 shows the evolution of the macroscopic failure stress for different values of the microscopic failure criterion. The stress evolved linearly. The macroscopic failure stress for silica is 50 *MPa*. The corresponding value of the failure criterion σ_f^{hyd} is approximately 64 *MPa*.

5.1. Convergence study

The mesh dependence of the failure criterion was investigated in the same way as the elastic parameter. Figure 9 shows the evolution of the macroscopic failure stress σ_{M_f} as the function of the number of discrete elements in the discrete sample. For this study the calibrated value of the failure criterion for silica glass $\sigma_f^{hyd} = 64$ *MPa* was used. The results showed a good stability of the macroscopic failure stress around the silica glass values of 50 *MPa*.

5.2. Validation tests

At this stage, only tensile tests were performed. The behavior induced by the failure criterion was validated by simulating bending and torsion tests for four distinct discrete samples. The table 1 summarizes the macroscopic failure stresses obtained from the tensile, bending and torsion tests. Fairly similar average macroscopic failure stresses were obtained from tensile, bending and torsion tests accordingly to the material strength theory.

The crack path for the numerical torsion tests were also observed. Figure 10 shows an image of the test results. The crack geometry conformed to the prediction by the material strength theory of a path along a helical

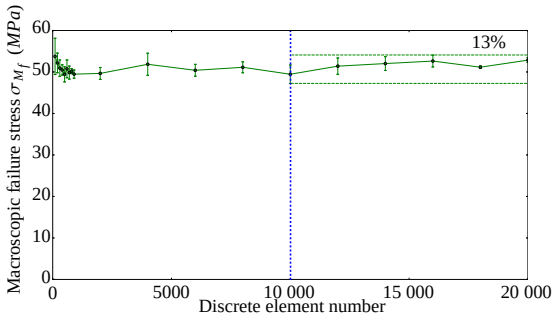

Figure 9: Evolution of the macroscopic failure stress σ_{M_f} as a function of the number of discrete element for a failure criterion $\sigma_f^{hyd} = 64\ MPa$.

Sample	Tensile	Bending	Torsion
n° 1	53.3 MPa	47.0 MPa	51.5 MPa
n° 2	48.0 MPa	47.0 MPa	47.6 MPa
n° 3	48.3 MPa	46.2 MPa	50.9 MPa
n° 4	48.2 MPa	55.5 MPa	47.7 MPa
average	49.5 MPa	48.9 MPa	49.4 MPa
std. deviation	2.2 MPa	3.8 MPa	1.8 MPa

Table 1: Overview of macroscopic failure stresses from tensile, bending and torsion tests; the four discrete samples used consisted of approximately 10 000 discrete elements.

surface oriented at 45° to the main axis of the cylindrical sample.

5.3. Conclusion

In this section, novel failure criterion was developed corresponding to the application of a maximal hydrostatic stress to the discrete elements. A preliminary study, involving qualitative indentation tests was used, to compare the standard criterion to the developed criterion in terms of the crack paths. The results using the developed criterion agreed with the experimental observations, while the standard criterion did not describe the experimental results accurately.

The calibration procedure for the microscopic failure criterion for silica glass was also described. The stability of the elastic parameters and the failure behavior were studied. The macroscopic failure stress was fairly independent of the sample morphology. Thus, if the discrete domain satisfied the geometric criteria (the geometric isotropy, the coordination number, the compacity and the fineness) the failure criterion could be considered to be independent of the discrete sample shape and mesh size.

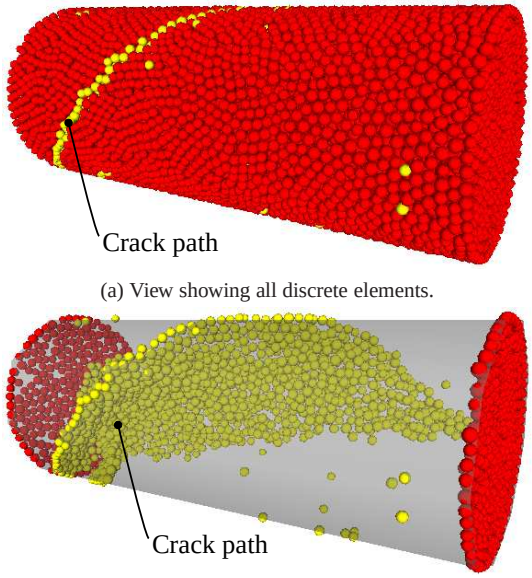

(a) View showing all discrete elements.

(b) View showing only critical discrete elements.

Figure 10: View of crack path in a torsion test; The highlighted discrete elements attained the failure criterion (critical discrete elements).

Finally, the failure criterion was validated by bending and torsion tests. The developed model adequately predicted the failure stress levels and the crack paths in comparison with the material strength theory. For completeness, more complex failure tests, known as indentation tests, are presented in the next section.

6. Application of the model to indentation tests with a spherical indenter

Figure 5 illustrates the crack geometry for an indentation test with a spherical indenter for loading a silica glass sample. Figure 11 shows an idealized view of the sample and the indenter and the associated parametrization, where :

- $\vec{P}$ denotes the indenter load,
- R denotes the indenter radius,
- d_c denotes the contact diameter indenter-sample,
- d denotes the cone surface diameter,
- l denotes the cone length and
- a denotes the cone angle.

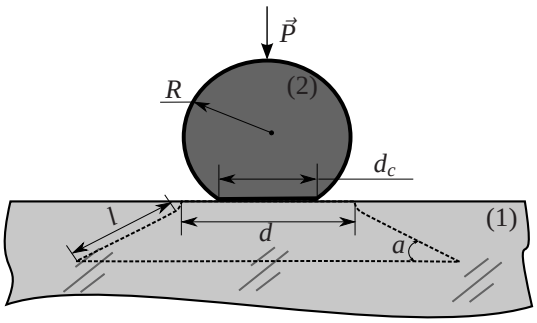

Figure 11: Idealized sketch and parametrization of a hertzian cone crack.

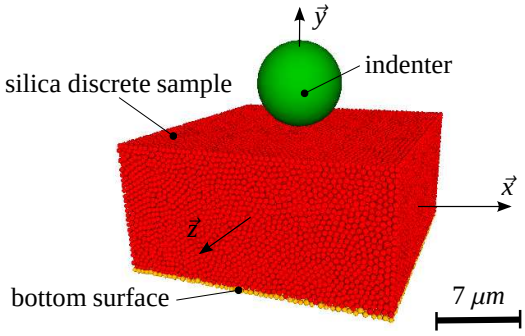

Figure 12: Discrete element model for the indentation test.

The simulation was based on the discrete element model described in this paper. Contact management between the indenter and the silica discrete sample was incorporated into this model.

6.1. Numerical method for indenter-sample contact management

The indenter is simulated by a single discrete element acting on the discretized silica glass sample. Figure 12 shows this configuration for the indenter and the sample. A constant velocity along the $-\vec{y}$ axis is applied to the indenter to load the discrete sample. The displacement along the $\vec{y}$ axis of the discrete elements belonging to the bottom face of the silica sample are forbidden. During its displacement, the indenter contacts some discrete elements on the upper face of the discrete sample. The reaction force induced by these elementary contacts are calculated using the hertzian contact law (33) :

$$\vec{f_{ij}} = \frac{4}{3} E^* \sqrt{R^* h_{ij}^3} \vec{u_{ij}} \tag{5}$$

$$\text{with : } \frac{1}{E^*} = \frac{1-\nu_i^2}{E_i} + \frac{1-\nu_j^2}{E_j} \tag{6}$$

$$\frac{1}{R^*} = \frac{1}{R_i} + \frac{1}{R_j} \tag{7}$$

where :

- i and j refer to two distinct discrete elements, one of which is always the indenter. The contacts between discrete elements of the silica sample are not take in account;
- $\vec{u_{ij}}$ is the unit vector between the centers of the two discrete elements, which are in contact;
- h_{ij} is the interpenetration between the two discrete elements i and j;
- E and ν are the Young's modulus and Poisson's ratio respectively and
- R_i is the radius of the discrete element i.

6.2. Overview of the simulation conditions

The discrete silica sample is composed by 80 000 discrete elements and 1 040 000 cohesive beams. Its size is 40 μm along the $\vec{x}$ and $\vec{z}$ axes and 20 μm along the $\vec{y}$ axis. The gravity was neglected. The time step is approximately 1.5 10^{-11} s. The total number of iterations for one simulation is approximately 80 000. A constant velocity was applied to the indenter. Its value was 0.3 $m.s^{-1}$. Dynamic effects were minimized by introducing a purely numerical damping factor into the numerical scheme as described in (34, 6).

6.3. Validation of elastic behavior

The model was first validated in terms of the elastic behavior. The theoretical evolution of the contact radius between the indenter and the sample was compared with the numerical data. The theoretical evolution of the contact radius was calculated using the hertzian contact law, which is given by (33):

$$a_c^{th} = \left(\frac{3}{4} \frac{PR}{E^*} \right)^{\frac{1}{3}} \tag{8}$$

The contact radius was "measured" in the simulation by recording the discrete elements in contact with the indenter. However, this procedure does not produce an exact measurement of the contact radius. The contact area is overestimated because of the contribution from the discrete elements at the boundary of this set. An underestimated contact area can be obtain by subtracting

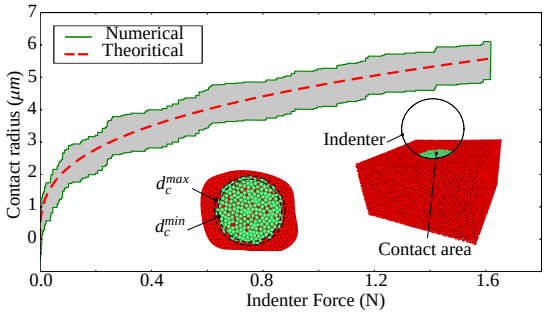

Figure 13: Theoretical and numerical evolution of the indenter contact radius with the indenter force.

Material	Diamond	
Young modulus	1054	*GPa*
Poisson's ratio	0.1	
Indenter radius	10	μm

Table 2: Overview of indenter properties.

Material	Silica glass	
Young modulus	72.5	*GPa*
Poisson's ratio	0.17	
Sample radius	50	*mm*
Sample thickness	5	*mm*

Table 3: Overview of sample properties.

Critical indenter load	P_f	200	*mN*
Cone angle	a	25-35	°
Cone length	l	8.0-9.2	μm
Cone diameter (at surface)	d	15.0	μm

Table 4: Characteristics of the experimentally observed hertzian cone.

the average value of the discrete element radii in this set from the contact area overestimate.

Figure 13 shows the evolution of the theoretical and the simulated contact radius with the indenter force. The maximal and minimal measured diameters of the contact area were d_c^{max} and d_c^{min}. The indenter force in the simulation is computed using :

$$P = -\sum_i \vec{f}_i.\vec{y} \tag{9}$$

Where $\vec{f}_i$ is the reaction force exerted by the the discrete element i on the indenter. In this figure, the gray area represents the margin between the overestimate and the underestimate contact radius. The red dashed line corresponds to the theoretical contact radius, which is bounded by the overestimate and the underestimate contact radius. The elastic behavior of the numerical indentation tests was therefore validated.

6.4. *Overview of experimental observations used as reference*

The work aims to further simulation techniques for glass polishing. The abrasive particles used to polish silica glass range in size from one micrometer to one hundred micrometers. Spherical indenters with a radius of ten micrometers were used in the indentation experiments to correspond to the order of magnitude of the size of practical abrasive particles.

The micro-indentation tests were carried out. The experimental procedure were similar to those described in (35, 36). Tables 2 and 3 list the properties of the indenter and the silica sample.

Figure 14 shows a hertzian crack in a fused silica sample. The images were obtained using confocal microscopy using the apparatus described in (37). After indentation, the imaging of the hertzian cone was felicitated by soaking the sample in a fluorescent dye, followed by thorough rinsing with DI water. This procedure enabled the dye to penetrate into the cracks to enable its visualization.

A preliminary statistical study was performed. The results showed that 90% of the hertzian cone cracks appeared at indenter loads bellow 500 *mN*. Each indenter print was examined to reject tests in which radial or lateral cracks happened that did not correspond to a hertzian cone crack. Hertzian cone cracks were produced for an indenter force range between 200 and 500 *mN*. This dispersion was attributed to the microscopic scale of the test. At this scale, small variations in parameters such as the surface roughness, the indenter erosion or the material default induced large variations in the results.

A test that produced a critical indenter load of 200 *mN* was chosen to compare numerical simulation results on the same order of magnitude as the experimental observation. Table 4 summarizes the characteristics of the chosen hertzian cone crack. These characteristics were obtaining by measuring several cross-sections of the cone because the experimental cone was not perfectly axisymmetric. Consequently, different measured values were obtained for different cross-sections.

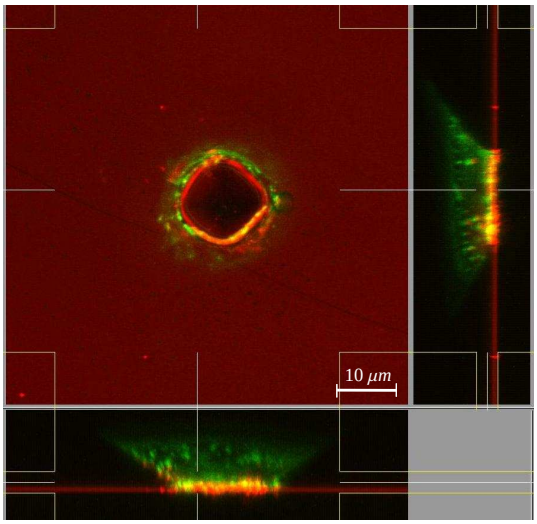

(a) 2D views : top view and side views

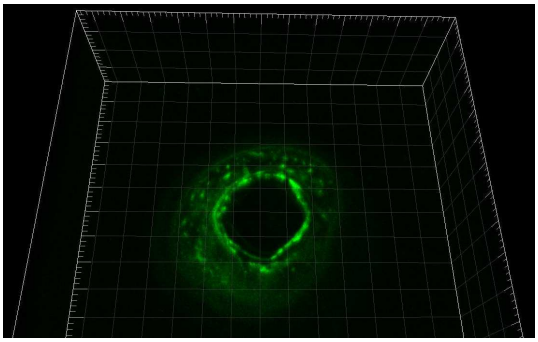

(b) 3D view

Figure 14: Image of a hertzian cone obtained by photo-luminescence microscopy; the surface color corresponds to the image in reflexion mode at 458 nanometers and the cone color corresponds to the image in fluorescence mode in the 435 to 661 nanometers spectral band for an excitation wavelength of 405 nanometers.

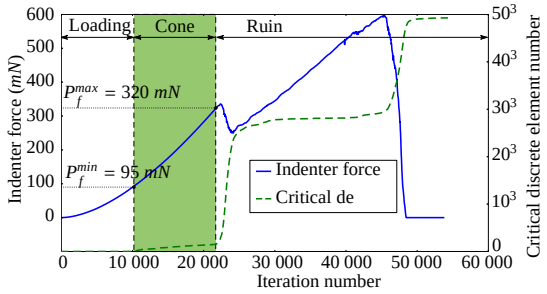

Figure 15: Evolution of the indenter force and the critical number of discrete elements with number of iterations.

6.5. *Indenter critical force P_f*

Figure 15 shows the evolution of the simulated indenter force and the critical discrete element number with the iteration number. The *critical discrete elements* are the discrete elements that attained the failure criterion. This graph shows the following three distinct zones:

1. the *loading* zone, in which no fracture occurred,
2. the *cone* zone, which corresponded to the hertzian cone generation as the number of critical discrete elements slowly increased,
3. the *ruin* zone, in which the discrete sample was destroyed as the number of critical discrete elements increased quickly and the indenter load decreased to a null value.

The indenter load corresponding to the beginning (P_f^{min} = 95 mN) and the ending (P_f^{max} = 320 mN) of the hertzian cone generation was on the same order of magnitude as the experimental observations. An exact concordance was difficult to obtain. A macroscopic failure stress of silica σ_f = 50 MPa has been established from macroscopic mechanical tests such as four bending point tests or tensile tests. This macroscopic value can be underestimated in micro-indentation tests, because of the extremely small loaded volume. Griffith hypothesized that, brittle material fractures are initiated by pre-existing micro or nano cracks (38). For lower activated volumes, the probability of the stress yield to open an pre-existing crack is lower and the resultant failure stress is higher than the macroscopic failure stress. This size effect is well known for concrete (39).

6.6. *Hertzian cone geometry*

In this section, the hertzian cone geometry in the simulation is compared to the experimentally observed geometry. The number of critical discrete elements at the

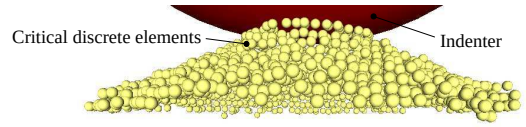

Figure 16: Picture of a simulated hertzian cone crack.

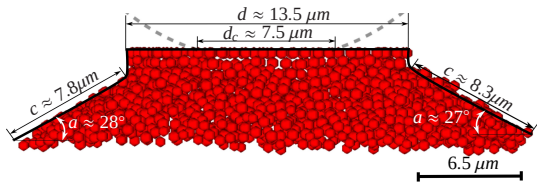

Figure 17: Characteristics of the simulated hertzian cone crack.

P_f^{min} value (see the previous section) was insufficient to observe the cone geometry. Figure 16 shows the critical discrete elements at approximately P_f^{max}. The hertzian cone was well-formed and could be compared to the experimental cone. Figure 17 shows the measured geometrical characteristics of the numerical cross-section that was used as a reference.

Table 5 summarizes the hertzian cone characteristics for the experimentally observed cone and the simulated cone. The simulated values agreed well with the experimental values.

7. Conclusion

A novel failure criterion was developed based on an equivalent hydrostatic stress for use in a spherical discrete element method. The advantage of this criterion is that is fairly independent of the sample morphology if the discrete domains satisfy the following geometric criteria : the geometrical isotropy, the cardinal number, the compacity and the fineness. In this case, a given set of microscopic parameter values could be associated with a simulated material. The calibration procedure was highly simplified by this property. The convergence of the results was also improved by significantly increasing the cardinal number of the discrete domain with a Delaunay triangulation process.

		Exp.	Num.	
Critical load	P_f	200	95-320	mN
Cone angle	a	25-35	27-28	°
Cone length	l	8.0-9.2	7.8-8.3	μm
Cone diameter	d	15.0	13.5	μm

Table 5: Comparison of the characteristics of the experimental and numerical observed cones.

The failure criterion was validated by torsion and bending tests. The results for the macroscopic failure stresses and the crack path geometries agreed qualitatively and quantitatively with the predictions of material strength theory.

Finally, this model was applied to a spherical indentation problem. The discrete model predicted a crack geometry similar to the experimentally observed geometry.

In conclusion, the proposed model is an interesting alternative for studying complex crack phenomena such as the generation of hertzian cone cracks.

8. Acknowledgments

This work was supported by the Conseil Régional d'Aquitaine and was conducted under the auspices of the Etude et Formation en Surfacage Optique (EFESO 2) project. The developments realized in this project were implemented in the GranOO[2] project.

References

[1] P. A. Cundall, O. D. L. Strack, A discrete numerical model for granular assemblies, Geotechnique 29 (1979) 47–65. doi:10.1680/geot.1979.29.1.47.

[2] S. Hentz, F. V. Donzé, L. Daudeville, Discrete element modelling of concrete submitted to dynamic loading at high strain rates, Computers & Structures 82 (29-30) (2004) 2509–2524. doi:10.1016/j.compstruc.2004.05.016.

[3] A. Bobet, A. Fakhimi, S. Johnson, J. Morris, F. Tonon, M. R. Yeung, Numerical models in discontinuous media: Review of advances for rock mechanics applications, Journal of Geotechnical and Geoenvironmental Engineering 135 (11) (2009) 1547–1561. doi:10.1061/(ASCE)GT.1943-5606.0000133.

[4] Y. Tan, D. Yang, Y. Sheng, Discrete element method (dem) modeling of fracture and damage in the machining process of polycrystalline sic, Journal of the European Ceramic Society 29 (6) (2009) 1029–1037. doi:DOI: 10.1016/j.jeurceramsoc.2008.07.060.

[5] I. Iordanoff, A. Battentier, J. Neauport, J. Charles, A discrete element model to investigate sub-surface damage due to surface polishing, Tribology International 41 (11) (2008) 957–964. doi:10.1016/j.triboint.2008.02.018.

[6] D. André, I. Iordanoff, J. luc Charles, J. Néauport, Discrete element method to simulate continuous material by using the cohesive beam model, Computer Methods in Applied Mechanics and Engineering 213–216 (0) (2012) 113 – 125. doi:10.1016/j.cma.2011.12.002.

[7] B. R. Lawn, , Journal of Material Research 19 (2003) 22–29. doi:10.1557/JMR.2004.0003.

[2] http://www.granoo.org

[8] H. A. Carmona, F. K. Wittel, F. Kun, H. J. Herrmann, Fragmentation processes in impact of spheres, Physical Review 77 (5) (2008) 051302. doi:10.1103/PhysRevE.77.051302.

[9] D. Potyondy, P. A. Cundall, A bonded-particle model for rock, International Journal of Rock Mechanics and Mining Sciences 41 (8) (2004) 1329–1364, rock Mechanics Results from the Underground Research Laboratory, Canada. doi:DOI: 10.1016/j.ijrmms.2004.09.011.

[10] T. Suratwala, P. Davis, L. Wong, P. Miller, M. Feit, J. Menapace, R. Steele, D. Walmer, Sub-surface mechanical damage distributions during grinding of fused silica, Journal of Non-Crystalline Solids 352 (2006) 5601–5617. doi:10.1016/j.jnoncrysol.2006.09.012.

[11] H. Hertz, Hertz's Miscellaneous Papers, Vol. 55, Macmillan, 1896, Ch. On hardness, 1882. doi:10.1038/055006f0.

[12] H. Hertz, Hertz's Miscellaneous Papers, Vol. 55, Macmillan, 1896, Ch. On the contact of elastic solid, 1881. doi:10.1038/055006f0.

[13] B. Lawn, T. Wilshaw, N. Hartley, A computer simulation study of hertzian cone crack growth, International Journal of Fracture 10 (1974) 1–16. doi:10.1007/BF00955075.

[14] P. Warren, Determining the fracture toughness of brittle materials by hertzian indentation, Journal of the European Ceramic Society 15 (3) (1995) 201 – 207. doi:10.1016/0955-2219(95)93941-U.

[15] C. Kocer, R. E. Collins, Angle of hertzian cone cracks, Journal of the American Ceramic Society 81 (7) (1998) 1736–1742. doi:10.1111/j.1151-2916.1998.tb02542.x.

[16] A. P. S. Selvadurai, Fracture evolution during indentation of a brittle elastic solid, Mechanics of Cohesive-frictional Materials 5 (4) (2000) 325–339. doi:10.1002/(SICI)1099-1484(200005)5:4<325::AID-CFM98>3.0.CO;2-K.

[17] G. Geandier, S. Denis, A. Mocellin, Float glass fracture toughness determination by hertzian contact: experiments and analysis, Journal of Non-Crystalline Solids 318 (3) (2003) 284 – 295. doi:10.1016/S0022-3093(02)01886-0.

[18] E. Rougier, A. Munjiza, N. W. M. John, Numerical comparison of some explicit time integration schemes used in dem, fem/dem and molecular dynamics, International Journal for Numerical Methods in Engineering 61 (6) (2004) 856–879. doi:10.1002/nme.1092.

[19] T. Pöschel, T. Schwager, Computational granular dynamics, Springer, 2005.

[20] S. P. Timoshenko, History of strength of materials: with a brief account of the history of theory of elasticity and theory of structures, Dover, New York, NY.

[21] K. Lochmann, L. Oger, D. Stoyan, Statistical analysis of random sphere packings with variable radius distribution, Solid State Sciences 8 (12) (2006) 1397–1413. doi:DOI: 10.1016/j.solidstatesciences.2006.07.011.

[22] M. de Berg, O. Cheong, M. van Kreveld, M. Overmars, Computational Geometry: Algorithms and Applications, Springer, 2008.

[23] R. Thomson, C. Hsieh, V. Rana, Lattice trapping of fracture cracks, Journal of Applied Physics 42 (8) (1971) 3154–3160. doi:10.1063/1.1660699.

[24] H. J. Herrmann, Random Fluctuations and Pattern Growth: Experiments and Models, NATO Advanced Study Institutes series. Series E, Applied sciences, Springer, 1988, Ch. Introduction to modern ideas on fracture patterns.

[25] E. Schlangen, J. G. M. van Mier, Experimental and numerical analysis of micromechanisms of fracture of cement-based composites, Cement and Concrete Composites 14 (2) (1992) 105–118, special Issue on Micromechanics of Failure in Cementitious Composites. doi:DOI: 10.1016/0958-9465(92)90004-F.

[26] M. Ostoja-Starzewski, Lattice models in micromechanics, Applied Mechanics Reviews 55 (2002) 35–60. doi:10.1115/1.1432990.

[27] F. A. Tavarez, M. E. Plesha, Discrete element method for modelling solid and particulate materials, International Journal for Numerical Methods in Engineering 70 (2007) 379–404. doi:10.1002/nme.1881.

[28] W. Shiu, F. V. Donze, L. Daudeville, Discrete element modelling of missile impacts on a reinforced concrete target, International Journal of Computer Applications in Technology 34 (1) (2009) 33–41. doi:doi:10.1504/IJCAT.2009.022700.

[29] P. A. K. Srivastava, Strength of Materials, PHI Learning Pvt. Ltd.

[30] F. C. Roesler, Brittle fractures near equilibrium, Proceedings of the Physical Society. Section B 69 (10) (1956) 981.

[31] M. Zhou, A new look at the atomic level virial stress: on continuum-molecular system equivalence, Proceedings of the Royal Society of London. Series A: Mathematical, Physical and Engineering Sciences 459 (2037) (2003) 2347–2392. doi:10.1098/rspa.2003.1127.

[32] B. Lawn, Fracture of brittle solids - second edition, Cambridge University Press, 1993.

[33] A. Fischer-Cripps, Introduction to Contact Mechanics, Mechanical Engineering Series, Springer, 2007.

[34] L. Mahéo, V. Grolleau, G. Rio, Damping efficiency of the tchamwa-wielgosz explicit dissipative scheme under instantaneous loading conditions, Comptes Rendus Mécanique 337 (11-12) (2009) 722–732. doi:doi:10.1016/j.crme.2009.10.005.

[35] J. Fournier, J. Néauport, P. Grua, V. Jubera, E. Fargin, D. Talaga, S. Jouannigot, Luminescence study of defects in silica glasses under near-uv excitation, Physics Procedia 8 (0) (2010) 39 – 43. doi:10.1016/j.phpro.2010.10.009.

[36] J. Fournier, J. Néauport, P. Grua, E. Fargin, V. Jubera, D. Talaga, S. Jouannigot, Evidence of a green luminescence band related to surface flaws in high purity silica glass, Optics Express 18 (21) (2010) 21557–21566, 10140 10140.

[37] J. Neauport, P. Cormont, P. Legros, C. Ambard, J. Destribats, Imaging subsurface damage of grinded fused silica optics by confocal fluorescence microscopy, Opt. Express 17 (5) (2009) 3543–3554. doi:10.1364/OE.17.003543.

[38] A. A. Griffith, The phenomena of rupture and flow in solids, Philosophical Transactions of the Royal Society of London 221 (1920) 163–198.

[39] Z. Bažant, J. Planas, Fracture and Size Effect: In Concrete and Other Quasibrittle Materials, New Directions in Civil Engineering Series, CRC PressINC, 1998.